OBS noise reduction from horizontal and vertical components using harmonic-percussive separation algorithms

Zahra Zali[1,2], Theresa Rein[1], Frank Krüger[1], Matthias Ohrnberger[1], Frank Scherbaum[1]

[1]University of Potsdam, Institute of Geosciences, Karl-Liebknecht-Str. 24-25, 14476 Potsdam, Germany

[2]GFZ German Research Centre for Geosciences, Potsdam, Germany

Correspondence to: Zahra Zali (zali@uni-potsdam.de)

Zahra Zali: Campus Golm, Building 29, Room 2.48, Karl-Liebknecht-Str. 24-25, 14476 Potsdam, Germany

(zali@uni-potsdam.de)

Theresa Rein: Campus Golm, Building 27, Room 0.43, Karl-Liebknecht-Str. 24-25, 14476 Potsdam,

Germany (theresa.rein@uni-potsdam.de)

Frank Krüger: Campus Golm, Building 27, Room 1.36, Karl-Liebknecht-Str. 24-25, 14476 Potsdam,

Germany (Frank.Krueger@geo.uni-potsdam.de)

Matthias Ohrnberger: Campus Golm, Building 27, Room 1.37, Karl-Liebknecht-Str. 24-25, 14476

Potsdam, Germany (Matthias.Ohrnberger@geo.uni-potsdam.de)

Frank Scherbaum: Campus Golm, Building 29, Room 1.52, Karl-Liebknecht-Str. 24-25, 14476 Potsdam,

Germany (Frank.Scherbaum@geo.uni-potsdam.de)

20   **Abstract**

21   Records from ocean bottom seismometers (OBS) are highly contaminated by noise, which is much higher

22   compared to data from most land stations, especially on the horizontal components. The high energy of the

23   oceanic noise at frequencies below 1 Hz complicates the analysis of the teleseismic earthquake signals

24   recorded by OBSs.

25   Previous studies suggested different approaches to remove low frequency noises from the data, but mainly

26   focused on the vertical component. The records of horizontal components, crucial for the application of

27   many methods in passive seismological analysis of body and surface waves could not be much improved in

28   the teleseismic frequency band. Here we introduce a noise reduction method, which is derived from the

29   harmonic-percussive separation algorithms used in Zali et al., (2021) in order to separate long-lasting

30   narrowband signals from broadband transients in the OBS signal. This leads to significant noise reduction

31   of OBS records on both the vertical and horizontal components and increases the earthquake signal to noise

32   ratio without distortion of the broadband earthquake waveforms. This is proved through synthetic tests by

33   measuring SNR and cross-correlation coefficient where both showed significant improvement for different

34   realistic noise realizations. The application of denoised signals in surface wave analysis and receiver

35   function is discussed through synthetic and real tests.

36

37   **1 Introduction**

38   Data from ocean bottom recordings are commonly difficult to analyze, due to the high noise level being

39   typically much higher compared to land stations. At frequencies below 1 Hz, the effect of the ocean noise is

40   often dominating the data and hinders the seismological analysis (e.g. Webb et al., 1991; Crawford, 1994).

41   Signals of interest, i.e. transient signals, especially from teleseismic events can be masked by the oceanic

42   noise. Here, the horizontal components are most strongly contaminated by low frequency noise. To

43   illustrate the noise on OBS data, we exemplary show the records of the station D10 of the DOCTAR array

44   (see Fig. 1 and Fig. S1). Various studies tried to identify and characterize the different sources of noise

45   recorded at the ocean bottom (e.g. Webb, 1998; Crawford & Webb, 2000; Corela, 2014; Stähler et al.,

46   2018; Essing et al., 2021; An et al., 2021). We focus on noise sources that especially affect teleseismic

47   horizontal recordings in the frequency band of 0.02–2 Hz. Generally, the dominant natural noise signals in

48   the oceanic environment are secondary oceanic microseisms (Rayleigh/Scholte waves at the ocean bottom)

49   caused by interaction of wind generated water waves, infragravity waves (compliance noise) as well as tilt

50   noise; the latter is originating from the turbulent interaction between currents and the instrument (e.g.

51   Crawford et al., 1998; Corela, 2014). Primary oceanic microseism is originating from the interaction of

52   water waves incident at steep coastlines and/or rough seafloor (Hasselmann, 1963; Webb, 1998; Bell et al.,

53   2015) and its spectrum peak is around 0.07 Hz (Friedrich et al. 1998) in the Northern Atlantic. The

54   secondary microseism, in contrast shows signal frequencies above 0.1–0.25 Hz, with a maximum spectral

55   peak around 0.14 Hz (Friedrich et al., 1998, Fig. 1) and is in general much stronger in amplitude than the

56   primary microseism. The secondary microseism is caused by wind or swell waves propagating in opposite

57   directions. The periods of such generated Rayleigh/Scholte-waves are half the period of the water waves
58   generating them (e.g. Longuet-Higgins, 1950; Bell et al., 2015) and strongly affect the seismological
59   analysis. Whereas the primary and secondary microseisms affect both the vertical and horizontal
60   seismometer components, the compliance noise is solely observed on the vertical component and the
61   hydrophone. Compliance noise, dominant in the frequency band of 0.01–0.04 Hz, is only significant if the
62   wavelength exceeds the water depth (Crawford et al., 1998; Crawford & Webb, 2000; Bell et al., 2015).
63   Below frequencies of 0.01 Hz and 0.1 Hz, the vertical and especially the horizontal components, are highly
64   contaminated by tilt noise generated by ocean bottom currents (Webb, 1998; Crawford& Webb, 2000;
65   Stähler et al., 2018, Fig. 1). The tilt noise level increases with signal period (see Fig. 1). The ocean bottom
66   currents in many regions of the oceans are mostly driven by tidal force and often create a signal with
67   strongest amplitudes below 1 Hz appearing every 6–12 hours (e.g. Brink, 1995; Crawford & Webb, 2000;
68   Ramakrushana Reddy et al., 2020; Essing et al., 2021). The ocean bottom currents passing the instrument
69   create local eddy currents, deform the seafloor beneath the sensor and tilt the whole instrument frame, to
70   which the seismometer is fixed (e.g. Duennebier & Sutton, 1995; Webb, 1998; Romanowicz et al., 1998;
71   Crawford & Webb, 2000; Corela, 2014; Stähler et al., 2018). If the seismometer mass is not perfectly
72   leveled, the high tilt noise on the horizontal components is partially projected onto the vertical component
73   (e.g. Crawford, 1994; Corela, 2014; Bell et al., 2015). Since the noise sources often act at frequencies of
74   teleseismic earthquakes, it is crucial to improve the Signal-to-Noise Ratio (SNR) on OBS recordings for the
75   analysis of the earth's crustal and mantle structure. Various studies discussed the improvement of OBS
76   recordings through different approaches, either by suggesting a better OBS instrument design (Stähler et
77   al., 2018, Corela, 2014, Essing et al., 2021), or by removing significant amounts of the noise from the
78   contaminated data by signal processing (Crawford & Webb, 2000, Bell et al., 2015, Janiszewski et al.,
79   2019). Our study follows the latter approach.
80   Crawford and Webb (2000) developed a method to remove noise from the vertical OBS component.
81   Calculating the linear transfer function between the horizontal and the vertical component allows to
82   estimate the tilt noise which can be subtracted from the vertical component. Hydrophone data measured in
83   parallel to the seismometer recordings allow to reduce the influence of infragravity waves on the vertical
84   seismometer component recordings. For better results Bell et al. (2015) propose to first rotate the horizontal
85   components in direction of the highest coherence between the horizontal and vertical component before
86   calculating the linear transfer functions. The mentioned methods solely improve the SNR on the vertical
87   component whereas the noise contamination on horizontal components is often larger. Other recent studies
88   attempted to reduce noise also on the horizontal components (Mousavi and Langston, 2017; Zhu et al.,
89   2019; An et al., 2021; Negi et al., 2021). An et al. (2021) tried to reduce the noise on the horizontal
90   components by applying the reversed procedure of Bell et al. (2015). Rotation of one horizontal component
91   into the direction of the principle noise indeed results in an improvement of the orthogonal horizontal
92   component, but the other horizontal component became noisier (An et al., 2021). Results of a recent study
93   applying a polarization filter to reduce the noise on all components show strong changes of the broadband

94 waveforms (Negi et al., 2021). The automatic noise-attenuation method developed by Mousavi and

95 Langston (2017) is a time-frequency denoising algorithm using the wavelet transform and

96 synchrosqueezing. It can be either used to keep the signal and remove the noise or vice versa. The

97 decomposition method DeepDenoiser from Zhu et al. (2019) is based on a deep neural network.

98 DeepDenoise decomposes the waveform into signal and noise in the time-frequency domain. The latter

99 methods, both improve the SNR, but mainly focus on local and regional earthquake detection and result in

100 changes in the waveform shape if the noise amplitude directly ahead of the signal is significant in

101 comparison to the signal amplitude in a specific frequency. However, the analysis of undistorted broadband

102 waveforms on the horizontal components is crucial for many passive seismological structure analysis

103 methods, e.g. receiver functions or surface wave dispersion and polarization analysis.

104 Here we introduce a method, inspired from the music information retrieval (MIR), which is adapted to

105 seismological data and is used for noise reduction on both, the vertical and the horizontal components.

106 Seismic waveform and acoustic signals generated by musical instruments are similar in some aspects

107 (Schlindwein et al., 1995; Johnson and Watson, 2019). The extensive research in the field of music

108 information retrieval has resulted in advances (e.g., Müller, 2015) that may be useful in seismic signal

109 processing as well. Exploiting the idea of harmonic-percussive separation (HPS) in MIR, Zali et al. (2021)

110 developed an algorithm to separate harmonic volcanic tremor from earthquakes in seismic waveforms. In

111 this study we use this algorithm after some modifications in order to separate 'harmonic' (long-lasting

112 narrowband signals) and 'percussive' (broadband transients) components of an OBS data set aiming at

113 noise reduction and retrieval of clearer broadband earthquake waveforms. Throughout this study we will

114 make use of the term noise for any signal other than earthquake signal in the data set. In the context of OBS

115 noise reduction using HPS algorithms, percussive components correspond to earthquake signals and

116 harmonic components correspond to noise signals. The long-duration OBS noise signals that last a few

117 hours to days (depending on the noise type) with a restricted frequency range contrasts with transient

118 seismic signals such as earthquakes with a wider range of frequencies.

119 The algorithm introduced in Zali et al., (2021) is a combination of two HPS approaches that leads to the

120 desired signal separation. Here we also use the two approaches in order to separate different type of noise

121 signals from the earthquake signals. In the first step we adopt HPS using a similarity matrix (Rafii and

122 Pardo, 2012; Rafii et al., 2014) to separate monochromatic and harmonic noises. In the second step we

123 adopt HPS using median filtering (FitzGerald, 2012) in order to separate the remaining narrow-band

124 signals. With this two-step approach we can separate and remove much of the OBS noise contamination

125 from the earthquake signals.

126

127 **2 Data**

128 In this study we discuss the noise recorded by a LOBSTER (Longterm OBS for Tsunami and Earthquake

129 Research) OBS instrument from the DEPAS pool, which is equipped with a Güralp CMG-40T

130 seismometer, a MCS (Marine compact seismic) recorder and loose cables (for technical specification see

131 the DEPAS Pool web page and Alfred-Wegener-Institute, Helmholtz-Zentrum für Polar- und
132 Meeresforschung et al., 2017). We show data recorded during the DOCTAR deployment, using DEPAS-
133 LOBSTERs, located around the Gloria Fault in the Northern Atlantic. Twelve DEPAS-LOBSTERs form
134 the array. They were deployed between 2011-2012 and recorded the data with a sampling frequency of 100
135 Hz (Hannemann et al., 2016; Hannemann et al., 2017).

136 Until 2019 the DEPAS LOBSTER OBS was built with an OBS-specific version of the Güralp CMG-
137 40T/MCS recorder, where the seismometer had a corner frequency of 60 s and has been modified to last
138 long on the seafloor (Stähler et al., 2018). However, the development of less power consumption lead to a
139 higher noise level of the instrument itself (Stähler et al., 2018). At low frequencies (<0.1 Hz) the self-noise
140 of the sensor is highly affecting the records, especially on the vertical component. However, the design of
141 the DEPAS-LOBSTERs has been improved for deployments after 2019 (e.g. Essing et al., 2021).

142 We observed a continuous harmonic signal at a frequency of 0.04 Hz, partially with one or two overtones
143 on a subset of the array (see Fig. 1). This signal was observed on 30% of the stations from the DOCTAR
144 project (e.g., Hannemann et al, 2016, Hannemann et al., 2017) and on 43% of the stations from the
145 KNIPAS project (Schlindwein et al., 2018), both using the mentioned DEPAS-LOBSTER design. We
146 cannot identify the source of this signal yet, but based on its continuity, we assume an electronic source
147 from the instrument itself.

148 The hydrophone and especially the horizontal components are highly affected by the strumming of the
149 head-buoy, which is attached to the DEPAS-LOBSTER frame causing a 'current induced harmonic tremor
150 signal' (Stähler et al., 2018; Essing et al., 2021, Fig. 1). These 'tremor events' last over up to 4 hours and
151 appear every 6–12 hours. These presumably tidal-driven tremor events are harmonic signals with a
152 fundamental period of 0.4–1 s and various overtones (1–10 Hz) (Stähler et al., 2018; Essing et al., 2021,
153 Fig. 1). Regarding the frequency band, 'tremor events' mainly affect the analysis of teleseismic body
154 waves, especially on the horizontal component (Fig. 1).

155

156 **3 Noise reduction methodology**
157
158 **3.1 Harmonic-percussive separation (HPS)**
159
160 Harmonic-percussive separation refers to the problem of decomposing a signal into its harmonic and
161 percussive components. This topic has received much attention in recent years (Rafii et al., 2018) and has
162 numerous applications in the field of MIR and musical signal processing.
163
164 Within a general context harmonic signals show an overtone structure in the spectral domain. We call
165 overtones one or more clear narrow-banded frequency peaks being integer multiples of the fundamental

166 frequency (the first frequency peak in the spectrum). Harmonic signals have a relatively stable behavior
167 over time and can be identified in a Short Time Fourier Transform (STFT) spectrogram by horizontal
168 structures referred to constant frequencies along the time axis.
169 In contrast percussive signals form vertical structures in a STFT spectrogram that contain energy in a wide
170 range of frequencies. Therefore it is a straightforward strategy in most HPS algorithms to try to separate the
171 horizontal structure from the vertical structure in the spectrogram corresponding to harmonic and
172 percussive components, respectively. The horizontal lines in the spectrogram could correspond to either
173 harmonic signals or monochromatic signals.
174
175 OBS noise forms narrowband horizontal structures in the STFT spectrogram while earthquake signals have
176 vertical exhibition in the STFT spectrogram.
177
178 **3.2 HPS using median filtering (MED)**
179
180 In the context of HPS one of the simplest and fastest approaches is median filtering (FitzGerald, 2010). For
181 simplification we name this algorithm as MED in this study. Median filters are usually used to remove
182 noise from an image or a signal. Using median filter a sample will be replaced by the median of
183 neighboring samples within a window of a specific length (The specific length is the kernel size of the
184 median filter). The entire signal is processed using a sliding window analysis. Within the HPS, two median
185 filters are applied to the amplitude of the STFT spectrogram of a signal. A median filter is performed along
186 the time axis of the spectrogram to suppress percussive events and enhance harmonic components. Another
187 median filter is applied along the frequency axis in order to enhance percussive events and suppress
188 harmonic components. The two resulting spectrograms are then subsequently used to create two masks,
189 which are applied to the original signal spectrogram separately to generate two spectrograms of harmonic
190 and percussive components. For creating the harmonic and percussive signals in time domain the phase of
191 the original signal is added to each spectrogram and the time domain signals are reconstructed using the
192 inverse STFT.
193
194 **3.3 HPS using the similarity matrix (SIM)**
195
196 Another powerful approach in HPS proposed by Rafii & Pardo (2012) is based on calculating a similarity
197 matrix. We name this algorithm as SIM here. This approach is a repetition-based separation, which
198 identifies the repeating elements by looking for similarities by means of a similarity matrix. Within the SIM
199 algorithm, first similar time frames in the spectrogram are identified through a similarity matrix. Then a
200 median filter is applied only to the frames identified as similar to constitute the repeating spectrogram
201 model that corresponds to harmonic components. The non-repeating spectrogram that corresponds to the
202 percussive component of the data is obtained by subtracting the repeating spectrogram from the original

203 spectrogram. For creating the repeating and nonrepeating signals in time domain the phase of the original

204 signal is added to each spectrogram and the time domain signals are reconstructed using the inverse STFT.

205 Details of this approach are discussed in the following section.

206

207 **3.4 HPS noise reduction algorithm for OBS data**

208

209 The motivation of using HPS for noise reduction of OBS data is originated from different characteristic of

210 earthquake and OBS noise signals as described in Sect. 2. Earthquakes are broadband transient signals,

211 while most of OBS noises are dominantly narrow-band signals and can be considered to have a

212 monochromatic or harmonic appearance in the spectrogram. We combine two modified HPS algorithms to

213 separate those signals in a two-step procedure. We divide the frequency content of the signal into two

214 ranges; one is between 0.1 to 1 Hz and the other is everywhere out of this frequency range. In the first step

215 we use the SIM algorithm and separate only harmonic or monochromatic signals from the original records

216 everywhere out of the mentioned frequency range. In the second step we target the specified frequency

217 range containing harmonic (or monochromatic) as well as narrow-band signals with gliding frequencies

218 named as current induced harmonic tremor signal in the Sect. 2 previously. The overall schematic diagram

219 of our HPS noise reduction algorithm along with an example is shown in Fig. 2.

220 The SIM algorithm is explained in the following: From the original OBS record SO (SO represents the

221 original restituted OBS signal) we derive the STFT named X being a complex-valued spectrogram.

222 The complex-valued spectrogram $\mathbf{X}$ is separated into its amplitude and phase components using Eq. 1.

223

$$X = V * exp(1j * \varphi), \qquad (1)$$

224

225 where φ is the phase of $\mathbf{X}$, $V = |\mathbf{X}|$ is the amplitude of X and j is the imaginary unit.

226 All of the spectrogram modifications will be done on the amplitude spectrogram $\mathbf{V}$. The cosine similarity

227 (the similarity between two vectors of an inner product space) between the STFT time frames is calculated

228 through the multiplication of the transposed $\mathbf{V}$ by $\mathbf{V}$ with normalization of the $\mathbf{V}$. This is shown in Eq. 2.

229

$$S(k_a, k_b) = \frac{\sum_{i=1}^{n} V(i, k_a) V(i, k_b)}{\sqrt{\sum_{i=1}^{n} V(i, k_a)^2} \sqrt{\sum_{i=1}^{n} V(i, k_b)^2}}, \qquad (2)$$

230

231 where $\mathbf{S}$ is the similarity matrix. Each point (k_a, k_b) in $\mathbf{S}$ is the cosine similarity between time frame k_a and

232 k_b of $\mathbf{V}$, $\forall k_{a,b} \in [1,m]$, where m is the number of time frames and n is the number of frequency channels

233 for each time frame. Once the similarity matrix is calculated we use it to determine the most similar time

234 frames to each single time frame. For time frame k_a we compare all the values in $\mathbf{S}(k_a, k_i)$ for $i \in [1,m]$.

235 2% of the all time frames, which have the highest S values, are identified as similar frames for time frame

236 k_a.

237 Finally, all similar time frames to any frame k in **V** are stored in a temporary array **K**. Those similar time

238 frames are used to create a repeating spectrogram model **W**. The corresponding frame in **W** is obtained by

239 taking the median of **K** for each frequency at each time frame k. Those time-frequency bins, which are

240 similar with little deviations between repeating frames, are captured by the median and constitute the

241 repeating spectrogram model. This spectrogram contains only similar and repeating patterns. The time-

242 frequency bins with large deviations between repeating frames would constitute nonrepeating transient

243 patterns and would be suppressed by the median filtering.

244

245 The nonnegative spectrogram **V** is the sum of two nonnegative spectrograms of repeating and nonrepeating

246 patterns, hence, **W** (the repeating spectrogram model) should always have smaller values or at most be

247 equal compared to **V**. To ensure this a repeating spectrogram model $\widetilde{\mathbf{W}}$ is defined by taking the minimum

248 between **W** and **V**. The nonrepeating spectrogram model is derived by subtracting $\widetilde{\mathbf{W}}$ from V.

249

250 We use these two (the repeating and the nonrepeating) spectrogram models to create two time-frequency

251 masks for repeating and nonrepeating patterns. Instead of the binary mask, which is used in Rafii & Pardo

252 (2012), we use soft masks via Wiener filtering (Vaseghi, 1996). The calculation of the soft masks is shown

253 in the following equations:

254

$$M1 = \frac{\widetilde{W}^2}{\widetilde{W}^2 + \left(V - \widetilde{W}\right)^2}, \tag{3}$$

$$M2 = \frac{\left(V - \widetilde{W}\right)^2}{\left(V - \widetilde{W}\right)^2 + \widetilde{W}^2}, \tag{4}$$

255

256

257 in which **M1** and **M2** are repeating and nonrepeating masks respectively. We multiply the masks with the

258 input amplitude spectrogram **V** to separate the repeating and nonrepeating components. The element-wise

259 multiplication of the masks by the input amplitude spectrogram **V** is shown in the following equations:

260

$$R = M1 \otimes V, \tag{5}$$

$$NR = M2 \otimes V, \tag{6}$$

261

262 in which **R** and **NR** denote repeating and nonrepeating amplitude spectrograms respectively.

263

264   The resulting **R** and **NR** spectrograms are shown in Fig. 2a for a specific/typical example of an OBS

265   recording. As can be observed in the **R** spectrogram, in particular the low frequency harmonic or

266   monochromatic signals below 0.1 Hz are well captured. We applied the SIM algorithm only to the

267   frequency band below 0.1 Hz and above 1 Hz. In the frequency band from 0.1 Hz to 1 Hz the signals

268   remains unchanged by this procedure. This is the first constraint we consider for the SIM algorithm. The

269   reason is related to the frequency content of the noise and earthquake signals and how the SIM algorithm

270   separates them. In the field of noise reduction using signal processing techniques, a very important point is

271   to not modify the signals of interest for analysis. P and S waveforms in the teleseismic earthquake signals

272   have often frequency content in the range of 0.1 Hz to 1 Hz with a dominant frequency around 0.3 Hz.

273   Oceanic microseism noise, which is usually present in the OBS data, has a dominant frequency around 0.1

274   Hz to 0.3 Hz. As P and S phases have similar dominant frequency as the microseism noise wavefield,

275   superposition of both wavefields could happen in this frequency range. They could interfere constructively

276   or destructively so the resulting amplitude could be higher or lower compared to the original P or S phase

277   amplitudes. Considering these interferences, using the SIM algorithm, may result in creating fake higher

278   amplitude for these phases or losing part of their amplitude in the noise reduced signal. But this could be

279   problematic only when the amplitude of the noise is changing over the time. For a noise signal with almost

280   constant amplitude, the SIM algorithm can extract the true amplitude of the noise even in the interference

281   moments. However, the microseism noise has slightly varying amplitude over time.

282

283   Before moving to the second step we introduce a second constraint parameter, which we use in the SIM

284   algorithm. Surface waves of teleseismic events show usually a dispersed narrow-band signal and

285   correspond to (on a daily scale) short duration mainly horizontal patterns in the spectrogram. Given the way

286   the HPS is separating harmonic from transient signals, the surface wavetrain may be erroneously

287   recognized as harmonic component and thus be separated as noise signal. In order to prevent this and

288   preserve the whole frequency content of the earthquake, we define a so-called waiting factor for the

289   similarity calculation introducing a minimum time distance between two consecutive similar frames. For

290   the problem of retaining teleseismic surface waves we found that a waiting time of at least two hours

291   prevents the algorithm to prune surface waves from the transient signal part. The rationale is that the

292   duration of a teleseismic event is usually less than two hours whereas the noise components have longer

293   duration. Using this waiting factor prevents separating any harmonic component of the earthquake signal as

294   noise component. As a side effect this constraint causes that short duration harmonic/monochromatic noise

295   signals won't be well captured, too. However, these types of signals are not common in OBS data (see the

296   Sect. 2).

297

298   In the second step of our algorithm, to target noise signals in the frequency range of 0.1 Hz to 1 Hz, we use

299   MED as it is described in the Sect. 3.2. We apply this second part of the noise removal procedure only to a

300   restricted frequency band of 0.1 Hz to 1 Hz. We don't apply MED for the frequency range below 0.1 Hz to

301 avoid an interference with the surface wave signals of teleseismic events that shall be retained. The
302 dominant noise in the mentioned frequency range is the current induced harmonic tremor signal (see the
303 Sect. 2).
304 First we create **X′** spectrogram which is equal to **X** in the mentioned frequency range and is equal to zero
305 out of this band. Then a horizontal median filter is applied to **X′** in order to separate harmonic components.
306 Near horizontal patterns will be captured by the median filter and will be separated in the harmonic
307 spectrogram **H**.
308 Now we have two separated spectrograms for noise signals: **R**, which is derived from the first step, and **H**,
309 which is derived from the second step. Summing these two spectrograms will build the noise spectrogram
310 **N**. Subtracting **N** from the input amplitude spectrogram **V** will construct the transient spectrogram **T**.
311 As can be seen in Fig. 2a in step 2, the dominant energy of the narrow-band signals with gliding
312 frequencies in the range of 0.1 Hz to 1 Hz (the current induced harmonic tremor noise as introduced in the
313 Sect. 2) is captured in the noise spectrogram **N**, but part of that is still remained in the transient spectrogram
314 **T**. The signals with changing frequency that don't form complete horizontal lines in the spectrogram are
315 difficult to be captured by our HPS algorithm so part of their energy remains in the final spectrogram.
316
317 **3.5 Reconstruct the denoised signal**
318 In order to reconstruct the noise-removed signal in time domain we must add phase information to the
319 spectrogram. We had separated the complex-valued spectrogram **X** into its amplitude **V** and its phase
320 component using Eq. 1 and all the further modifications have been applied to the amplitude spectrogram **V**.
321 The phase of input signal SO is mostly affected by the phase of noise signals as they have the dominant
322 energy in the signal. Therefore we use phase information of SO in order to reconstruct the noise signal. We
323 add this phase to the noise spectrogram **N** using the following equation:
324

$$N' = N * exp(1j * \varphi), \qquad (7)$$

325

326 where **N′** is the complex-valued noise spectrogram. We reconstruct the noise signal *NS* from the complex
327 spectrogram **N′**, using the inverse STFT. Finally the OBS denoised signal HPS (HPS here represents the
328 SO signal after the HPS processing) is obtained by subtracting the noise signal from the input OBS signal
329 SO using the following equation:
330

$$HPS = SO - NS, \qquad (8)$$

331

332 **3.6 Parameters selection**
333

10

334   Many typical noise signals observed at OBSs are harmonic, monochromatic or narrow-band signals with

335   gliding frequencies (see the Sect. 2). In order to extract the expected narrowband noise signals from the

336   STFT we require a high frequency resolution in the spectral domain therefore making it necessary to use

337   sufficiently long time windows for the spectral analysis. Here we use an FFT window length of 163.84

338   seconds with an overlap of 75%, corresponding to an FFT size of 16384 at a sampling frequency of 100 Hz,

339   which corresponds to a frequency resolution of 0.006 Hz.

340   We use a standard kernel size of 80 for the median filter in the MED algorithm. The larger the kernel size,

341   the more noise signal would be captured. Our tests show that a kernel size of 80 is the largest size, which

342   leads to a safe separation without capturing any energy of the earthquake signal.

343

344   **4 Results and Discussion**

345

346   **4.1 General Results**

347

348   In this section we aim to prove the reliability of our HPS noise reduction algorithm and evaluate the

349   improvement of the OBS data. We applied the method to synthetic and real teleseismic earthquake data

350   recorded by the OBS station D10 of the DOCTAR array (e.g., Hannemann et al, 2016, Hannemann et al.,

351   2017). The synthetics were calculated for a source-receiver epicentral distance of 40° (focal depth: 45 km,

352   focal mechanism: double couple, source duration: 4 s) by using the full wavefield software qseis (Wang,

353   1999) and a modified average ak135 velocity model including a water layer (Kennett et al, 1995). The

354   crustal structure of the velocity model is adapted to the 11.5 km deep oceanic crust in that area and the

355   water depth is fixed to 5 km. Real oceanic noise of the ZRT components recorded by the station D10 is

356   added to the corresponding components of the synthetic teleseismic signal. We created synthetics for three

357   different noise scenarios at the beginning (N1), during (N2) and after (N3) tidal currents (Fig. 3) each with

358   theoretical SNR of 1–10 between noise and P-onset on pure synthetic Z. Throughout the whole paper the

359   SNR is defined as root mean square (RMS) of the signal divided by RMS of the noise. For further details of

360   synthetic data creation see Fig. S2. For the comparison with real data, we selected in total 46 teleseismic

361   events with Magnitudes Mw >5.6 and epicentral distances of 30–160° (see Fig. S1). Here only those

362   events were used, where a P onset could be visually identified. The pre-selection of the events is taken from

363   Hannemann et al. (2017) and expanded by some events with low magnitudes (see Table S1). In the

364   following, we will discuss the improvement of the records by comparing the seismograms and

365   spectrograms of synthetic data and confirm it with real data. We also verify the improvement for two

366   seismological applications (teleseismic surface wave group velocity analysis and receiver function

367   analysis). For some observations, e.g. checking the phase arrival of the teleseismic body waves, we rotated

368   the arbitrary orientated horizontal components of the real data into the ZRT system. The orientation angles

369   are taken from the previous study on the DOCTAR array (Hannemann et al., 2016).

370

371   Comparing the spectrograms and waveforms of the synthetic example a significant improvement of the
372   SNR is seen in the HPS processed data set on all components (e.g. Fig. 3 and Fig. S3–5 for the real data).
373   The continuous spectral lines of the assumed electronic noise are removed from the data, as well as most of
374   the spectral lines related to tremor episodes of head-buoy strumming. During the tides, we observe a
375   reduction of the spectral amplitudes for the tilt noise, as well as for the general background noise (Fig. 3
376   and Fig. S3–5) on the horizontal components. The results concluded from the spectrograms are confirmed
377   by the spectra (Fig. 2b), which show the removal of the spectral peaks of the electronic noise (0.05, 0.1,
378   0.15 Hz) and the tremor episodes (0.5–1 Hz). The amplitudes of the frequencies corresponding to the
379   teleseismic event and its waveforms are maintained (see Fig. 3).
380   To quantify the improvements of the method, we calculated the cross-correlation of the teleseismic
381   waveform, the SNR of the teleseismic body-wave phases and the RMS of the teleseismic waveform before
382   and after denoising. Because most of the oceanic noise ranges at frequencies below 1 Hz, which is also the
383   most interested frequency range of the OBS analysis, a 1 Hz low pass filter is applied to the signals before
384   all result calculations.
385   We calculated the correlation coefficient for synthetic SO and HPS compared with the synthetic earthquake
386   signal for different SNR and noise realizations and plotted it in Fig. 4a. The high correlation coefficients for
387   HPS and synthetic compared with SO and synthetic in all cases demonstrate that HPS denoising preserves
388   the earthquake signal and doesn't introduce waveform distortion.
389   For the SNR calculation we used a signal window of 30 s starting from the theoretical onset (direct P on Z
390   component, direct S on R and T component and Love wave on the T component) and a noise window of 60
391   s starting 70 s before the theoretical onset. For the Love wave, the SV phase (R component) and P phase (Z
392   component) the SNR increased significantly (Fig. 4b). For SH phase on T component we observe a few
393   apparent SNR decreases comparing SO with HPS traces (Fig. 4b). The SNR is calculated on the noise
394   contaminated SO traces, it hence compares noise with noise contaminated synthetic signal. Because of this
395   and because we added the synthetics amplified according to SNR for P-arrival on Z component to the real
396   noise, in a few cases we observe apparent SNRs slightly below 1 for a few SH phases (see Fig. 4b).
397   The RMS amplitudes of a noise free R component synthetic, SO and HPS signals are estimated over 8
398   seconds windows with 80% overlap and plotted in Fig. 4c. Comparing the RMS amplitude of the synthetic,
399   SO and HPS we see that the synthetic and HPS have similar amplitude ranges while SO has a much higher
400   amplitude. This shows a significant noise reduction in HPS along with preserving the earthquake energy.
401   As there is some noise remaining after denoising we see some differences in the overall shapes of the RMS
402   amplitude of the synthetic and HPS (especially after minute 24 which is almost at the end of the energy of
403   the synthetic signal), however HPS shows peaks on the arrival times of seismic phases of the synthetic
404   which means that the energy of seismic phases is preserved after denoising. The minor changes in seismic
405   phase shapes of the synthetic and HPS is also due to remaining noise. The seismograms and spectrograms
406   related to this example are presented in Fig. 3. Figure 4d shows a comparison of RMS amplitude of the
407   original noise in SO (blue curve), the remaining noise in HPS after denoising (red curve) and the synthetic

408 earthquake (green curve) signals. Besides a high noise reduction in HPS, the plot shows that the remaining
409 noise is independent from the pattern of the synthetic earthquake, which confirms that denoising process
410 doesn't affect the earthquake energy in the HPS signal.
411
412 **4.2 Applications**
413 By applying our HPS noise reduction algorithm, we aim to improve seismological analysis, especially
414 those involving the analysis of teleseismic body and surface waves. Valuable constraints of the Earth's
415 structure in oceanic regions can be taken from the analysis of the SH-wavefield like Love-waves, which are
416 not influenced by the water column, but often cannot be analyzed due to strong noise on the horizontal
417 components. SV waves are also often masked by noise, but are for instance important for tomography
418 studies or S and SKS shear wave splitting analysis (e.g. Silver and Chan, 1991). Other techniques using the
419 SV-wavefield like the Z/R ratio of the teleseismic Rayleigh waves (Tanimoto & Rivera, 2008), or receiver
420 functions (RF) (Langston, 1979) also rely on clear radial component readings. In the following we will
421 show the improvement which was achieved for the SH arrivals and for the group velocity analysis of
422 teleseismic Rayleigh- and Love waves, as well as for the receiver function analysis.
423
424 **4.2.1 SH-waves**
425 Since SH-waves are weak in energy and displayed on the noise-contaminated transversal horizontal
426 component (T), they are sparsely observable on OBS data and mostly disappeared behind the high noise
427 level. However, on the HPS processed data we see an improvement of the SNR on the T-component (see
428 Fig. 4b). In many cases the SH-phase is clearly identifiable on the HPS T-component (see Fig. 3d for a
429 synthetic data and Fig. S6 for a real data example).
430
431 **4.2.2 Surface waves**
432 Rayleigh waves in deep oceanic domains are strongly influenced by the water column, because most of the
433 wave energy is traveling in the water. This poses a problem, if the water depth changes along the travel
434 path. Love waves are not influenced by the water column but are recorded only on horizontal components
435 and their recordings on OBS systems are therefore more disturbed by strong noise sources like tilt inducing
436 tidal currents. To test the performance of the HPS noise reduction algorithm in the long period range, we
437 performed a measurement of group velocities of Love and Rayleigh waves with the Multiple Filter
438 Technique (MFT) (Dziewonski et al., 1969). Group velocity curves are for instance used as input data for
439 tomographic studies to reveal the 3D structure of the lithosphere and upper mantle. Figure 5 shows group
440 velocity curves for the synthetic Love wavetrain for the three noise situations N1-N3. For the MFT analysis
441 we used the software mft96 (Herrmann, 2013). The unfiltered seismograms in the top panels (Fig. 5a–c)
442 correspond to the P-wave SNR = 1 scenario. In all three cases the clarity of the dispersion curve is greatly
443 enhanced in the images resulting from the HPS processed traces (Fig. 5e–g) in comparison to the noise free
444 image (Fig. 5d). Also the seismogram traces improved greatly. The dispersion maps show that also noise

445   energy in the range of the signal frequencies is removed successfully in the frequency range 0.05 to 0.2 Hz.
446   Longer signal periods which are weakly visible in the noise-free image (Fig. 5d) can not be recovered. The
447   corresponding results for the Rayleigh wavetrain on the radial component are shown in Fig. S7. For the N3
448   case here also longer periods down to 40 s can be successfully denoised.
449   For an evaluation of the HPS denoising technique on real surface wave data we selected 23 events with
450   magnitudes larger than Mw 6.0 in the distance range between 47.5° and 159.6° and added one event with
451   Mw= 5.6 at a distance of 37.9° (see Fig. S1). Figure S8 shows seismograms and MFT analysis examples
452   for three events with different magnitudes and in different distances. The resulting group velocity
453   dispersion curves for all 24 events for the original and processed data are shown in Fig. S9. For all
454   components we find that the improved signal to noise ratio of the processed data allows the analysis of
455   more events and of a broader period range than in the original data.
456
457   **4.2.3 Receiver Functions**
458   Receiver functions have been proven to be a valuable tool to observe the Earth's structure using teleseismic
459   events (e.g., Langston, 1979, Ammon et al., 1995, Kind et al., 1995; Rondenay, 2009). Separating the
460   source site from the receiver site by deconvolution allows to estimate the Earth's structure beneath the
461   station. Here, we compare the receiver functions calculated from the synthetic examples and from real data
462   before and after denoising (Fig. 6). The synthetics used for the receiver function calculation are pure
463   synthetic signals contaminated by real noise (N1, N2, N3). On the synthetics, the SNR for P ranges
464   between 1–10 (for detailed description of the synthetic creation, see Sect. 4.1, Fig. 3 and S2). Receiver
465   function analysis and the observation of the Earth's structure beneath the DOCTAR array was already
466   calculated by Hannemann et al. (2017). Here, we don't aim to estimate the crustal and mantle structures,
467   instead we aim to compare the P-receiver Functions of the radial component calculated from the original
468   synthetic and real data (SO R-RF) with receiver functions of the radial component from the HPS processed
469   synthetic and real data (HPS R-RF). To calculate the receiver functions, we applied the iterative
470   deconvolution in the time domain (Ligorría & Ammon, 1999). We corrected the data for the Ps-phase,
471   quality controlled (e.g. P-onset at 0 s on Z of HPS R-RF), stacked and low-pass filtered the synthetic data at
472   2 Hz and bandpass filtered the traces between 0.05–0.5 Hz for the real data with a zero-phase Butterworth
473   filter. For both synthetic and real receiver function, the noise level strongly decreased and we observe a
474   significant decrease in variance on the HPS traces compared to the SO traces (Fig. 6).
475   Our result shows that determination of the crustal- and mantle-phases is more reliable on the HPS R-RF
476   stack than on the SO R-RF stack for both synthetic and real data (Fig. 6). We observe more distinct Ps-
477   phase arrivals on the HPS R-RF than on the SO R-RF stack. The Ps-phases are caused by the P-to-S
478   conversion at the Mohorovičić-, 410-km and 660-km discontinuity (hereafter referred to as Moho, 410, and
479   660, respectively; e.g. Deuss, 2009). For the synthetic example, we expect the P-to-s conversion at the
480   Moho at depths of 11.5 km to arrive at 0.8s, which is better resolved in the synthetic HPS R-RF than in the
481   synthetic SO R-RF, same for it's multiple ($P_{M}sPp$) and the water multiples every 6.5s (M_{WATER}, Fig. 6a).

482   Assuming ak135 velocities we would expect the $P_{410}s$-phase (Ps conversion at the 410) to arrive at around

483   43 s and the $P_{660}s$-phase (Ps conversion at the 660) at around 66.8 s delayed to the direct P-arrival (see Fig.

484   6 a & b).

485

486   Instead of a rather weak peak on the SO-R-RF real data stack we observe a strong peak at around 43 s, with

487   a good SNR on the HPS R-RF stack, indicating the sharp velocity contrast at the 410 (Fig. 6b). Comparing

488   the SO-RF and the HPS-RF real data stacks, the amplitudes of the $P_{660}s$-phase decreased and became a

489   broader peak, which we would expect from a conversion at a more gradual velocity contrast at the 660 (Fig.

490   6b). These results are in line with the analysis of the crustal and mantle structure beneath the DOCTAR

491   array presented by Hannemann et al. (2017). The negative phase (X1 in Fig. 6b) arriving at around 5 s is

492   stronger on the HPS-R-RF real data stack than on the SO-R-RF real data stack and might either indicate the

493   PpSs multiple of the Ps-phase at the Moho, or the direct P-to-s conversion at the LAB. On the HPS-R-RF

494   real data stack we observe a strong positive phase (X2) arriving at 12 s (Fig. 6b). This phase has not been

495   identified by Hannemann et al. (2017) and a detailed analysis of its origin is beyond the scope of this study,

496   but it might be related to the water multiples.

497   In general, receiver functions of OBS data are difficult to analyze and although the SNR of the HPS

498   processed data has been improved, the analysis of the real data is still difficult, especially compared to

499   receiver functions from land stations.

500

501   **5 Conclusions**

502

503   In this work we have developed a method to separate the signals of teleseismic earthquakes from other

504   signals in the OBS data resulted in noise reduction of OBS data. Our method is a combination of two HPS

505   algorithms from the field of MIR to separate harmonic and percussive components of an OBS data.

506   Earthquake signals as percussive components are separated from noise signals as harmonic components.

507   The noise signal is reconstructed using the phase information of the original signal. Subtracting the noise

508   signal from the original signal derives the noise-reduced signal. We discussed the motivation of using a two

509   step HPS approach, that results in a clean noise-reduced signal where the teleseismic broadband earthquake

510   waveforms are preserved with their whole frequency content. We also discussed the type of noise signals,

511   which are eligible for our noise reduction algorithm that contains most of the OBS noise energy.

512   The extracted noise signal contains some different signals where each can be derived by applying a band

513   pass filter to the extracted noise signal in a proper frequency band. The derived signal may be used in

514   researches related to that signal. For example the microseism signal can be extracted and used for

515   investigation of the source generation area of microseisms.

516

517   The comparison of original and HPS noise reduced synthetic signals shows how significantly the SNR has

518   improved after applying our method (Fig. 4b). However, the apparent SNR improvement highly depends on

519   the noise type characteristics. For Noise type 1 (N1), it seems like there is no SNR improvement on the T-
520   component (Fig. 4b, the second panel). N1 is taken from the beginning of the tidal current event, where we
521   have a considerable time dependent change in noise-frequencies. In this example, the noise has similar
522   frequencies with the signal. The visual inspection of the corresponding trace indicates a clear improvement
523   of the waveform for SH-wave on T component, even though the SNR shows no improvement. The results
524   from the cross-correlation (Fig. 4a), confirm the improvement and preservation of the waveform. Since we
525   are focusing on the preservation of the waveform and the SNR comparison highly depends on the noise
526   situation, the SNR should not solely be used to evaluate the improvement by HPS noise reduction method.
527   Even if the SNR is not improving in a few cases, the analysis of the cross-correlation, RMS and the pure
528   waveforms, verify the improvement of the traces by the HPS noise reduction method. From our analysis of
529   the broadband seismograms, we find out that the improvement is significant and may allow a broader and
530   more reliable analysis of teleseismic earthquake data. Applications like the receiver function technique and
531   SH-wave and Love wave analysis are considerably improved after applying the HPS noise reduction
532   algorithm. For the receiver function, we could observe a more distinct phase for the P-to-S conversion at
533   the Moho for the synthetic case and at the 410 km discontinuity for the real data. Group velocity analysis of
534   teleseismic surface wavetrains showed that application of the HPS noise reduction technique allows to
535   analyze more events and to analyze them in a broader frequency range. Especially more and wider Love
536   wave dispersion curves could be recovered. The noise reduction algorithm improves the horizontal
537   components significantly, which allows the OBS community to apply a broader range of seismological
538   methodologies, including the horizontal components, to the OBS-data.
539   In conclusion, the presented method is a powerful algorithm for separation and extraction of different
540   signals from OBS data and has especially application in noise reduction of OBS signals.

541   **Code and data availability**

542   The Python code related to the proposed method along with an example of real data is freely available from
543   https://github.com/ZahraZali/NoiseCut. A Jupyter notebook with all the Python codes and parameters relat-
544   ed to the proposed method is available as an electronic supplement. The sea floor seismological data were
545   archived by Alfred Wegener Institute (AWI), Helmholtz Centre for Polar Research, Bremerhaven, Germa-
546   ny, and are available upon request. The supplementary material related to this article contains list of all
547   earthquakes used in this study and a map showing their location. The illustrations of the semi-synthetic data
548   generation are presented in the supplementary material as well. An example of three components seismo-
549   gram and spectrogram before and after applying HPS noise reduction algorithm to real data, Rayleigh wave
550   group velocity analysis for a synthetic example, MFT analysis for three real events and group velocity
551   curves for some real events are also presented through figures in the supplementary material.
552
553   **Author contribution**

554 Z.Z. developed the algorithm and designed the study. T.R. created the synthetics data, conducted the
555 synthetic tests, and measured the receiver functions. F.K. conducted the group velocity analysis. Z.Z., T.R.,
556 and F.K. evaluated the results. Z.Z. and T.R. wrote the initial draft. All authors wrote the final manuscript
557 and discussed the results.
558

559 **Competing interests**

560 The authors declare that they have no conflict of interest.

575 **References**

576 Alfred-Wegener-Institut, Helmholtz-Zentrum für Polar- und Meeresforschung et al.: DEPAS (Deutscher
577 Geräte-Pool für amphibische Seismologie): German Instrument Pool for Amphibian Seismology, Journal of
578 largescale research facilities, 3, A122, https://doi.org/10.17815/jlsrf-3-165, 2017.
579

580 Ammon, C. J., Randall, G. E., & Zandt, G.: On the nonuniqueness of receiver function inversions, J.
581 Geophys. Res.-Sol Ea., 95(B10), 15303-15318, https://doi.org/10.1029/JB095iB10p15303, 1990.
582

583 An, C., Cai, C., Zhou, L., & Yang, T.: Characteristics of Low-Frequency Horizontal Noise of Ocean-
584 Bottom Seismic Data, Seismol. Res. Lett., https://doi.org/10.1785/0220200349, 2021.
585

586 Bell, S. W., Forsyth, D. W., & Ruan, Y.: Removing noise from the vertical component records of ocean-
587 bottom seismometers: Results from year one of the Cascadia Initiative, B. Seismol. Soc. Am., 105(1), 300-
588 313, https://doi.org/10.1785/0120140054, 2015.
589

590   Beyreuther, M., Barsch, R., Krischer, L., Megies, T., Behr, Y., Wassermann, J.: ObsPy: A Python
591   Toolbox for Seismology. Seismol. Res. Lett., 81(3), 530-533, 2010.

592   Brink, K. H.: Tidal and lower frequency currents above Fieberling Guyot. J. Geophys. Res.-:
593   Oceans, 100(C6), 10817-10832, https://doi.org/10.1029/95JC00998, 1995.

595   Corela, C.: Ocean bottom seismic noise: applications for the crust knowledge, interaction ocean-
596   atmosphere and instrumental behaviour. Ph.D. thesis, University of Lisbon, 339 pp, 2014.

598   Crawford, W. C.: Determination of oceanic crustal shear velocity structure from seafloor compliance
599   measurements (Doctoral dissertation, University of California, San Diego), 1994.

601   Crawford, W. C., & Webb, S. C.: Identifying and removing tilt noise from low-frequency (< 0.1 Hz)
602   seafloor vertical seismic data. B. Seismol. Soc. Am., 90(4), 952-963, https://doi.org/10.1785/0119990121,
603   2000.

605   Crawford, W. C., Webb, S. C., & Hildebrand, J. A.: Estimating shear velocities in the oceanic crust from
606   compliance measurements by two-dimensional finite difference modeling. J. Geophys. Res. -Sol Ea.,
607   103(B5), 9895-9916, https://doi.org/10.1029/97JB03532, 1998.

609   Deuss, A.: Global observations of mantle discontinuities using SS and PP precursors. Surv.
610   Geophys., 30(4-5), 301-326, https://doi.org/10.1007/s10712-009-9078-y, 2009.

612   Duennebier, F. K., & Sutton, G. H.: Fidelity of ocean bottom seismic observations, Oceanographic
613   Literature Review, 10(43), 996, 1995.

615   Dziewonski, A., S. Bloch, and M. Landisman.: A technique for the analysis of transient seismic signals, B.
616   Seismol. Soc. Am., 59, no. 1, 427-444, https://doi.org/10.1785/BSSA0590010427, 1969.

618   Essing, D., Schlindwein, V., Schmidt-Aursch, M. C., Hadziioannou, C., & Stähler, S. C.: Characteristics of
619   Current-Induced Harmonic Tremor Signals in Ocean-Bottom Seismometer Records, Seismological Society
620   of America, 92(5), 3100-3112. , https://doi.org/10.1785/0220200397, 2021.

622   Eulenfeld, T.: rf: Receiver function calculation in seismology, Journal of Open Source Software, 5(48),
623   1808, https://doi.org/10.21105/joss.01808, 2020.

625   Fitzgerald, D.: Harmonic/percussive separation using median filtering, In Proceedings of the International
626   Conference on Digital Audio Effects (DAFx) (Vol. 13), 2010.

627

628   FitzGerald, D.: Vocal separation using nearest neighbours and median filtering, 23rd IET Irish Signals and

629   Systems Conference, Maynooth. 28-29th. June 2012, https://doi.org/10.1049/ic.2012.0225, 2012.

630

631   Friedrich, A., Krüger, F., & Klinge, K.: Ocean-generated microseismic noise located with the Gräfenberg

632   array, J. Seismol., 2(1), 47-64, 1998.

633

634   Gaspà Rebull, O., Cusí, J. D., Ruiz Fernández, M., & Muset, J. G.: Tracking fin whale calls offshore the

635   Galicia Margin, north east Atlantic Ocean, The Journal of the Acoustical Society of America, 120(4), 2077-

636   2085, https://doi.org/10.1121/1.2336751, 2006.

637

638   Griffin, O. M.: Vortex-Induced Vibrations of Marine Cables and Structures, NRL Memorandum Report

639   5600, Naval Research Laboratory – Marine Technology Division, Washington D.C, 1985.

640

641   Hannemann, K., Krüger, F., Dahm, T., & Lange, D.: Structure of the oceanic lithosphere and upper mantle

642   north of the Gloria fault in the eastern mid-Atlantic by receiver function analysis, J. Geophys. Res-Sol Ea.,

643   122(10), 7927-7950, https://doi.org/10.1002/2016JB013582, 2017.

644

645   Hasselmann, K.: A statistical analysis of the generation of microseisms. Rev. Geophys., 1(2), 177-210,

646   https://doi.org/10.1029/RG001i002p00177, 1963.

647

648   Heimann, S., Kriegerowski, M., Isken, M., Cesca, S., Daout, S., Grigoli, F., Juretzek, C., Megies, T.,

649   Nooshiri, N., Steinberg, A., Sudhaus, H., Vasyura-Bathke, H., Willey, T., Dahm, T.: Pyrocko - An open-

650   source   seismology   toolbox   and   library.   V.   0.3.   GFZ   Data   Services,

651   https://doi.org/10.5880/GFZ.2.1.2017.001, 2017.

652

653   Herrmann, R. B.: Computer programs in seismology: An evolving tool for instruction and research, Seism.

654   Res. Lettr., 84, 1081-1088, https://doi.org/10.1785/0220110096, 2013.

655

656   Janiszewski, H. A., Gaherty, J. B., Abers, G. A., Gao, H., & Eilon, Z. C.: Amphibious surface-wave phase-

657   velocity   measurements   of   the   Cascadia   subduction   zone. Geophys.   J.   Int., 217(3),   1929-1948,

658   https://doi.org/10.1093/gji/ggz051, 2019.

659

660   Johnson, J. B., & Watson, L. M.: Monitoring volcanic craters with infrasound "music", Eos, 100.

661   https://doi.org/10.1029/2019EO123979, 2019.

662

663 Kennett, B. L., Engdahl, E. R., & Buland, R.: Constraints on seismic velocities in the Earth from trav-
664 eltimes. Geophys. J. Int., 122(1), 108-124, 1995.

666 Kind, R., Kosarev, G. L., & Petersen, N. V.: Receiver functions at the stations of the German Regional
667 Seismic Network (GRSN). Geophys. J. Int., 121(1), 191-202, https://doi.org/10.1111/j.1365-
668 246X.1995.tb03520.x, 1995.

670 Langston, C.A.: Structure under Mount Rainier, Washington, inferred from teleseismic body waves. J.
671 Geophys. Res., 84, 4749-4762, 1979.

673 Ligorría, J. P., & Ammon, C. J.: Iterative deconvolution and receiver-function estimation. B. Seismol. Soc.
674 Am., 89(5), 1395-1400, https://doi.org/10.1785/BSSA0890051395, 1999.

676 Longuet-Higgins, M. S.: A theory of the origin of microseisms, Philosophical Transactions of the Royal
677 Society of London. Series A, Mathematical and Physical Sciences, 243(857), 1-35,
678 https://doi.org/10.1098/rsta.1950.0012, 1950.

680 McFee, B., V. Lostanlen, A. Metsai, M. McVicar, S. Balke, C. Thomé, C. Raffel, F. Zalkow, A. Malek,
681 Dana, et al.: librosa/librosa: 0.8.0, Version 0.8.0, Zenodo, https://doi.org/10.5281/zenodo.3955228, 2020.

683 Mousavi, S. M., & Langston, C.A.: Automatic noise-removal/signal-removal based on general cross-
684 validation thresholding in synchrosqueezed domain and its application on earthquake data. Geophysics,
685 82.4, V211-V227. https://doi.org/10.1190/geo2016-0433.1, 2017.

687 Müller, M.: Fundamentals of music processing: Audio, analysis, algorithms, applications. Cham,
688 Switzerland: Springer International Publishing. https://doi.org/10.1007/978-3-319-21945-5, 2015.

690 Negi, S. S., Kumar, A., Ningthoujam, L. S., & Pandey, D. K.: An Efficient Approach of Data Adaptive
691 Polarization Filter to Extract Teleseismic Phases from the Ocean-Bottom Seismograms. Seismological
692 Society of America, 92(1), 528-542, https://doi.org/10.1785/0220200034, 2021.

694 Olofsson, B.: Marine ambient seismic noise in the frequency range 1–10 Hz. The Leading Edge, 29(4),
695 418-435, https://doi.org/10.1190/1.3378306, 2010.

697 Pereira, A., Romagosa, M., Corela, C., Silva, M. A., & Matias, L.: Source Levels of 20 Hz Fin Whale
698 Notes Measured as Sound Pressure and Particle Velocity from Ocean-Bottom Seismometers in the North

699   Atlantic. Journal of Marine Science and Engineering, 9(6), 646, https://doi.org/10.3390/jmse9060646,
700   2021.

701

702   Pillet, R., Deschamps, A., Legrand, D., Virieux, J., Béthoux, N., & Yates, B.: Interpretation of broadband
703   ocean-bottom seismometer horizontal data seismic background noise, B. Seismol. Soc. Am., 99(2B), 1333-
704   1342, https://doi.org/10.1785/0120080123, 2009.

705

706   Rafii, Z., Liutkus, A., & Pardo, B.: REPET for background/foreground separation in audio. In Blind Source
707   Separation (pp. 395-411). Springer, Berlin, Heidelberg, 2014.

708

709   Rafii, Z., Liutkus, A., Stöter, F. R., Mimilakis, S. I., FitzGerald, D., & Pardo, B.: An overview of lead and
710   accompaniment separation in music, IEEE/ACM Transactions on Audio, Speech, and Language
711   Processing, 26(8), 1307-1335. https://doi.org/10.1109/TASLP.2018.2825440, 2018.

712

713   Rafii, Z., & Pardo, B.: Music/Voice Separation Using the Similarity Matrix, Proc. ISMIR, pp. 583-588,
714   2012.

715

716   Ramakrushana Reddy, T., Dewangan, P., Arya, L., Singha, P., & Kamesh Raju, K. A.: Tidal triggering of
717   the harmonic noise in ocean-bottom seismometers. Seismol. Res. Lett., 91(2A), 803-813,
718   https://doi.org/10.1785/0220190080, 2020.

719

720   Rondenay, S.: Upper mantle imaging with array recordings of converted and scattered teleseismic waves.
721   Surv. Geophys., 30(4), 377-405, https://doi.org/10.1007/s10712-009-9071-5, 2009.

722

723   Romanowicz, B., Stakes, D., Montagner, J. P., Tarits, P., Uhrhammer, R., Begnaud, M., Stutzmann, E.,
724   Pasyanos, M., Karczewski, J.F., Etchemendy, S. and Neuhauser, D.: MOISE: A pilot experiment towards
725   long term sea-floor geophysical observatories, Earth, planets and space, 50(11), 927-937, 1998.

726

727   Schlindwein, V., Krüger, F., Schmidt-Aursch, M.: Project KNIPAS: DEPAS ocean-bottom seismometer
728   operations in the Greenland Sea in 2016-2017, Alfred Wegener Institute, Helmholtz Centre for Polar and
729   Marine Research, Bremerhaven, PANGAEA, https://doi.org/10.1594/PANGAEA.896635, 2018.

730

731   Schlindwein, V., Wassermann, J., & Scherbaum, F.: Spectral analysis of harmonic tremor signals at Mt.
732   Semeru volcano, Indonesia, Geophys. Res. Lett., 22(13), 1685-1688. https://doi.org/10.1029/95GL01433,
733   1995.

734

735 Skop, R. A., & Griffin, O. M.: On a theory for the vortex-excited oscillations of flexible cylindrical
736 structures. Journal of Sound and Vibration, 41(3), 263-274, https://doi.org/10.1016/S0022-460X(75)80173-
737 8, 1975.
738
739 Silver, P.G. & Chan, W.W.: Shear wave splitting and subcontinental mantle deformation. J. Geophys. Res.,
740 96, 16429-16454, 1991.
741
742 Snodgrass, F. E., Hasselmann, K. F., Miller, G. R., Munk, W. H., & Powers, W. H.: Propagation of ocean
743 swell across the Pacific, Philosophical Transactions of the Royal Society of London. Series A,
744 Mathematical and Physical Sciences, 259(1103), 431-497, https://doi.org/10.1098/rsta.1966.0022, 1996.
745
746 Stähler, S. C., Schmidt-Aursch, M. C., Hein, G., & Mars, R.: A self-noise model for the German DEPAS
747 OBS pool. Seismol. Res. Lett., 89(5), 1838-1845, https://doi.org/10.1785/0220180056, 2018.
748
749 Tanimoto, T., Rivera, L.: The ZH ratio method for long-period seismic data: sensitivity kernels and
750 observational techniques. Geophys. J. Int., 172(1), 187-198, https://doi.org/10.1111/j.1365-
751 246X.2007.03609.x, 2008.
752
753 Titze, I. R.: Nonlinear source–filter coupling in phonation: Theory, The Journal of the Acoustical Society
754 of America, 123(4), 1902-1915, https://doi.org/10.1121/1.2832337, 2008.
755
756 Vaseghi, S. V.: Advanced signal processing and digital noise reduction. Vieweg + Teubner Verlag, 1996.
757
758 Wang, R.: A simple orthonormalization method for stable and efficient computation of Green's
759 functions, B. Seismol. Soc. Am., 89(3), 733-741, https://doi.org/10.1785/BSSA0890030733, 1999.
760
761 Webb, S. C.: Broadband seismology and noise under the ocean, Rev. Geophys., 36(1), 105-142,
762 https://doi.org/10.1029/97RG02287, 1998.
763
764 Webb, S. C., Zhang, X., & Crawford, W.: Infragravity waves in the deep ocean, J. Geophys. Res.-:
765 Oceans, 96(C2), 2723-2736, https://doi.org/10.1029/90JC02212, 1991.
766
767 Zali, Z., Ohrnberger, M., Scherbaum, F., Cotton, F., & Eibl, E. P.: Volcanic Tremor Extraction and
768 Earthquake Detection Using Music Information Retrieval Algorithms, Seismol. Res. Lett., 92(6), 3668-
769 3681, https://doi.org/10.1785/0220210016, 2021.
770

771 Zhu, W., Mousavi, S. M., & Beroza, G. C.: Seismic signal denoising and decomposition using deep neural
772 networks. IEEE T. Geosci. Remote., 57(11), 9476-9488. https://doi.org/10.1109/TGRS.2019.2926772,
773 2019.

774
775
776

777
778
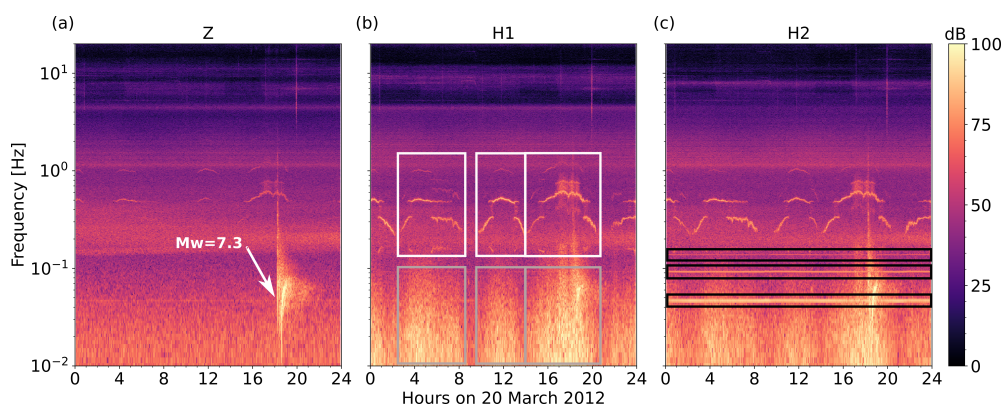
Figure 1: Spectrogram of an one-day OBS signal shows ocean bottom noise on Z (a), H1 (b) and H2 (c) components. The data was recorded by the station D10 of the DOCTAR array with a sampling frequency of 100 Hz. The spectrogram were calculated using a window length of 2^{16} sample and an overlap of 75%. The signal of an earthquake (Mw=7.3) on 20.3.2012 at around 18:00 at the station D10 is shown in (a). The tidal cycle of the current-induced noise is clearly visible during the high tilt noise episodes (grey box in b). The white box in (b) highlights the tremor episodes caused by the head buoy strumming. On H2 (c) we see an instrument-related, presumably electronic noise (black boxes). The high energy of the secondary microseism band at around 0.2 Hz is visible on all components.

787
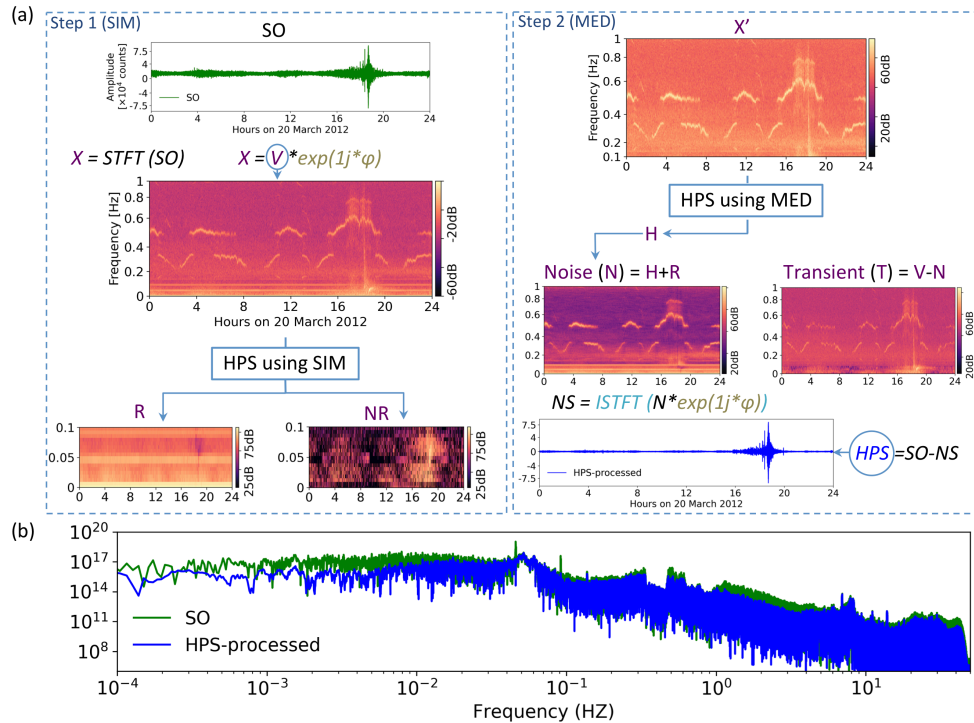
Figure 2: Method flowchart (a) Illustration of the processing steps with a real data example. Left panel shows the first step of the method where using the similarity matrix (SIM) in the frequency range below 0.1 Hz and above 1 Hz, we divide the spectrogram of the signal into two spectrograms of repeating (R) and non-repeating (NR) patterns. Right panel shows the second step of the method where we apply a median filter (MED) to the frequency range of 0.1 to 1 Hz in order to remove noises from this frequency range. As the interested frequency range for OBS signals is below 1 Hz, the spectrograms show only this frequency range. Finally the noise spectrogram (N) is created by summing the separated noises derived from two steps and the noise signal (NS) is derived using ISTFT. We obtain the noise reduced signal (HPS) by subtracting the NS from the input OBS signal (SO). STFT, short time Fourier transform. HPS, harmonic-percussive separation. SIM, similarity matrix. MED, median filtering. ISTFT, Inverse Short Time Fourier Transform. (b) Spectrum of the original signal (SO) and the HPS noise reduced signal.
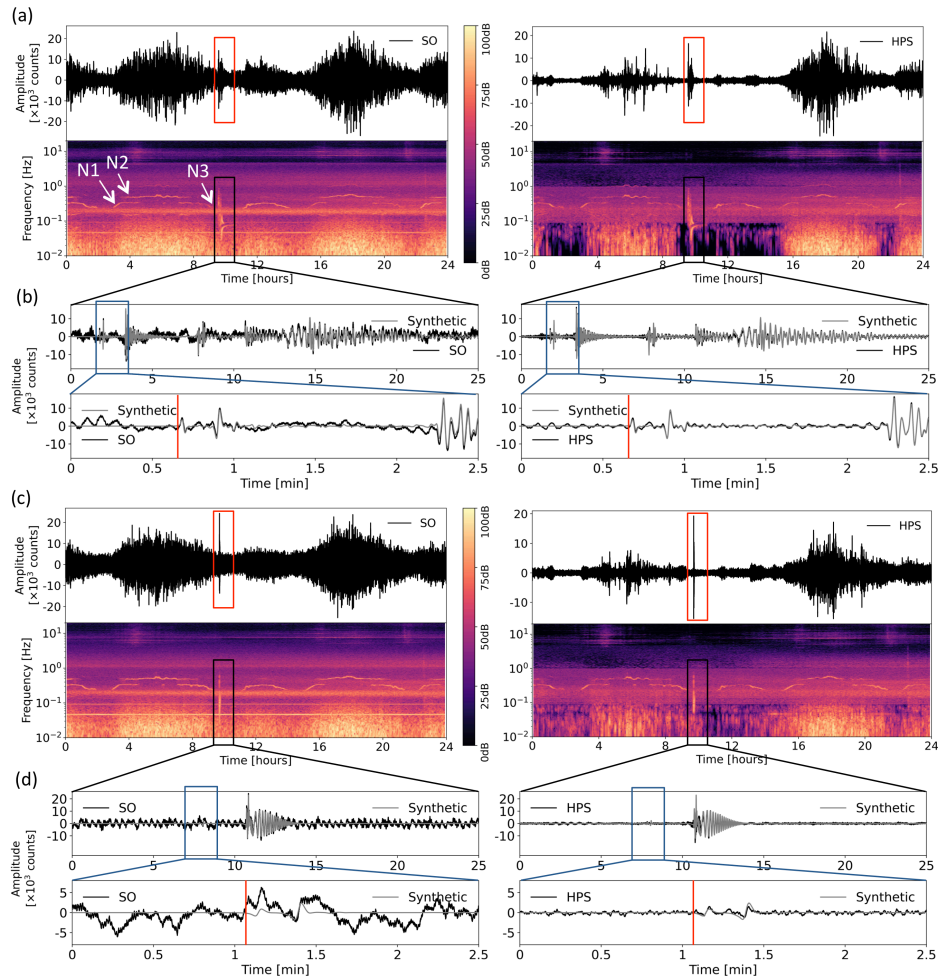
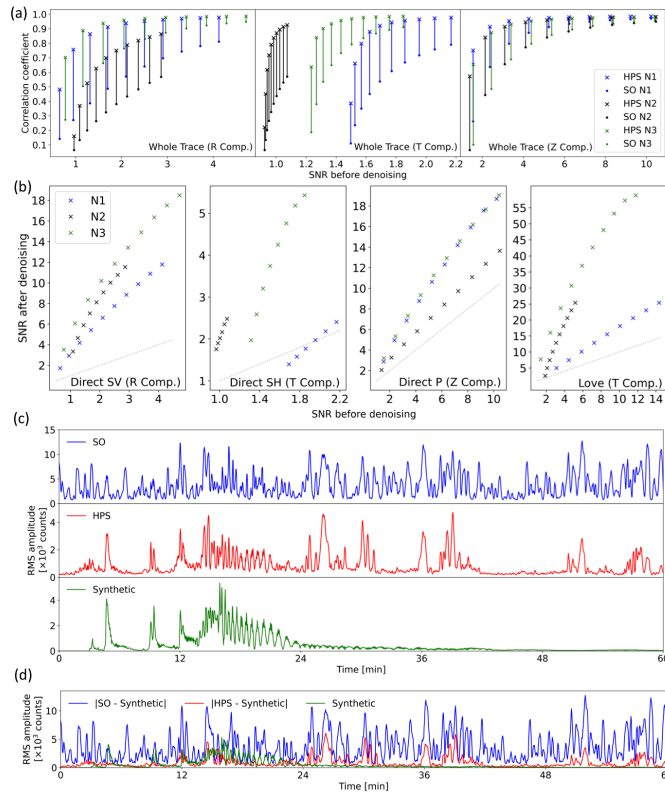**Figure 3: Comparison of the synthetic seismograms and spectrograms of the original signal SO and the HPS noise reduced signal on the R and T components for a synthetic signal with SNR= 1.5 before denoising (SNR is defined as RMS of the signal divided by RMS of the noise). (a) & (c) Show one day seismograms and spectrograms for R and T components, respectively. The spectrograms clearly show the reduced noise level on the HPS signal. Squares show the earthquake section. The arrows in (a) show three noise situations (N1-N3). (b) & (d) Show seismograms of the earthquake section on SO and HPS signals, with detailed view of the P-arrival (on component R in subfigure b) and SH-arrival (on component T in subfigure d). The whole amplitude and the phase information of the synthetic earthquake are preserved in the HPS signal but it's very less noisy compared with SO. Red lines show P-arrivals in (b) and SH-arrival in (d).**

816

817

818 **Figure 4: Comparison of the synthetic SO and HPS signals (both are lowpass filtered at 1Hz). (a) Correlation**
819 **coefficients (for the whole trace) for different SNRs and 3 realistic noise realizations for Z, R and T components**
820 **(Component is abbreviated as Comp.). (b) Improvement of SNR for direct body wave phases and the Love wave.**
821 **We see significant improvement in both correlation coefficient and SNR for all the realizations after denoising.**
822 **The gray dotted lines in (b) mark the line with gradient 1 (no improvement of SNR). (c) Comparison of the root**
823 **mean square (RMS) amplitude of one example of the SO, HPS and synthetic earthquake signals. The HPS signal**
824 **has significantly lower energy compared with SO due to noise reduction, but has almost similar energy**
825 **compared with the synthetic earthquake which shows the energy of the earthquakes and all the phase arrivals**
826 **are well preserved during the denoising process. This signal is the same example shown in Fig. 3 (R component,**
827 **SNR= 1.5 before denoising). (d) The RMS of the original noise (blue trace: |SO - Synthetic|) and the remained**
828 **noise after denoising (red trace: |HPS- Synthetic|) compared to the synthetic earthquake signal. A high noise**
829 **reduction is seen in the red trace compared with the blue one and the remained noise has an inconsistent pattern**
830 **compared to the synthetic earthquake that confirms denoising process doesn't modify the earthquake energy**
831 **and its phase arrivals.**
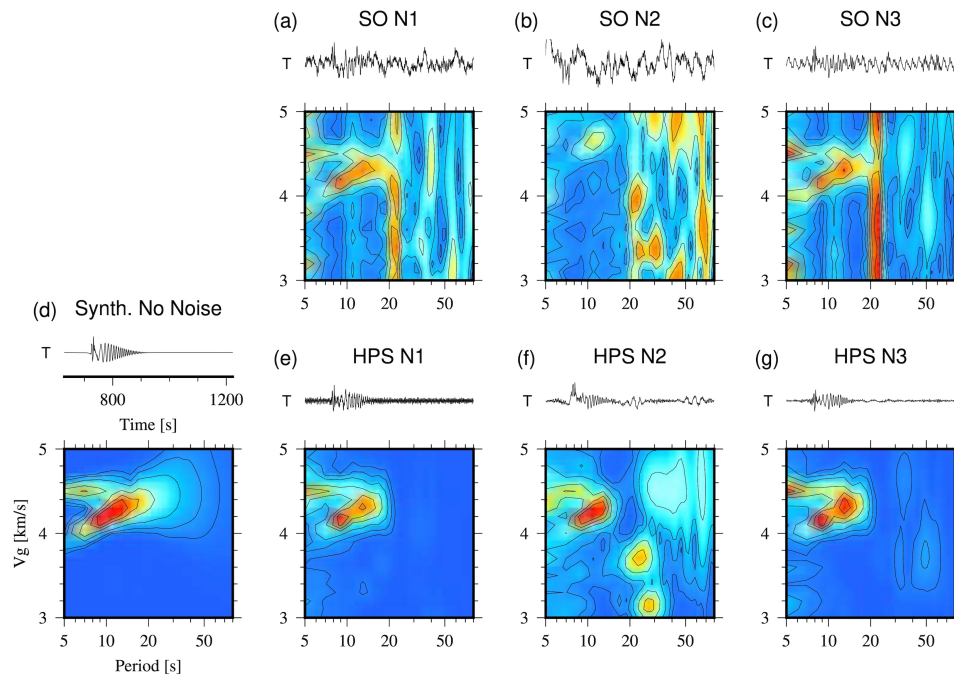
Figure 5: Love wave group velocity analysis for unfiltered and HPS processed synthetic Love wavetrains contaminated by three real world OBS noise signals (noise signals N1-N3, station D10, DOCTAR experiment, see Sect. 2 for more details). (a)–(c): Lower panels: Unfiltered synthetic signal (SO) MFT analysis results. Top panels: seismogram time windows corresponding to the range of group velocities shown on the y-axis. (d) Noise free synthetic case. (e)–(g): HPS processed input traces for noise situations N1-N3 (lower panel: MFT analysis result, top panel: HPS processed seismogram).
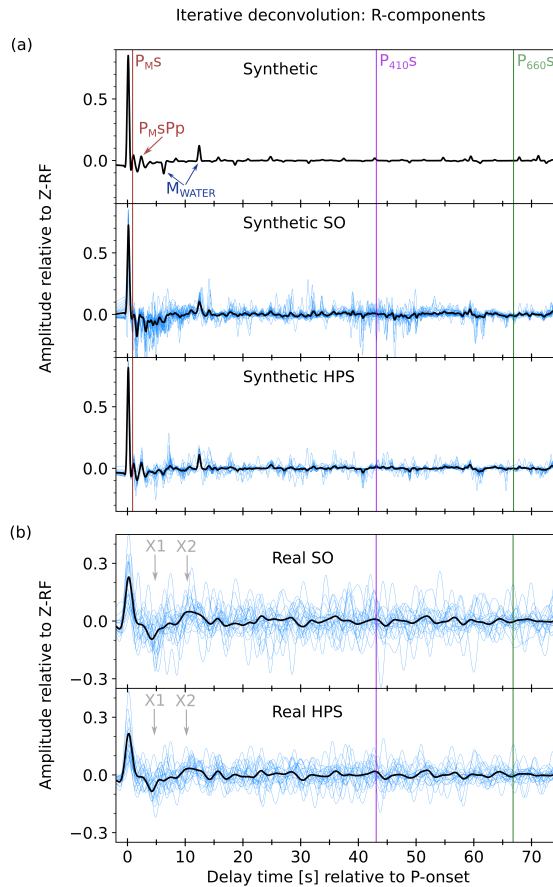
Figure 6: R-receiver function comparison of synthetic and real data examples. (a) Comparison of the synthetic data examples, lowpass filtered at 2 Hz. The pure synthetic R-RF is shown in the uppermost panel, followed by the synthetic SO and the synthetic HPS R-RFs. The black lines show the summed individual R-RFs (blue waveforms). The theoretical onset times for this specific model are marked. Red line: Ps-arrival of the Moho (P_MS) and its multiple (P_MsPp), violet line: Ps arrival of the 410 ($P_{410}s$), green line: Ps-arrival of the 660 ($P_{660}s$), dark-blue arrows: Multiples in the watercolumn of 4.9 km (M_{WATER}), repetitive every 6.5s. (b) Comparison of the real data, bandpass filtered at 0.05–0.5 Hz. The upper panel shows the R-RFs of the real SO traces and the lowermost panel the R-RFS of the real HPS traces. The individual traces (blue) are shown as stack (black line) and the theoretical onset times based on the average ak135 velocity model are shown as violet line ($P_{410}s$) and green line ($P_{660}s$). The origin of the phases X1 and X2 (grey) remain unclarified, since their interpretation is beyond the scope of this study.